J. Fluid Mech. (1970), *vol.* 43, *part* 2, *pp.* 305–319
Printed in Great Britain

The break-up of axisymmetric liquid sheets

By J. C. P. HUANG†

Department of Mechanical Engineering, Washington State University, Pullman, Washington 99163

(Received 10 November 1969 and in revised form 29 January 1970)

The break-up mechanism of axisymmetric liquid sheets formed by the impingement of two co-axial jets has been examined. Three break-up regimes in the Weber number range from 100 to 3×10^4 are reported. In the first break-up regime, droplets are formed through successive mergings of liquid beads along the nearly circular periphery of the sheet. The formation of beads is caused by Rayleigh instability. In the transition regime, Taylor's cardioid wave pattern prevails in the first half of this regime, while the sheet begins to flap in the second half.

In the second break-up regime, antisymmetric waves on the sheet grow radially. A semi-empirical equation has been deduced to predict the break-up radius of the sheet. The motion of an axisymmetric vibrating membrane with radially decreasing thickness has been studied to include Helmholtz instability as an analogue of the wave motion of the expanding circular sheet. A distorted progressive wave equation has been solved by the WKBJ method to indicate the effect of cylindrical geometry. The calculated wave speed agrees fairly well with experimental data at low Weber numbers.

1. Introduction

A general increasing interest in the behaviour of 'water bells' is evident in today's fluid mechanics literature. The thinning sheets that result when a jet strikes an obstacle or another jet, and the sprays that they ultimately break into, both have broad application. They are used for droplet control in combustion processes, and for their grace and beauty in fountains; they are used in garden sprinklers and for the application of a uniform coating.

Since Savart (1833) first observed the break-up radii of flat sheets that spread from two equal co-axial colliding jets over a century ago, there was a steady trickle of work on their behaviour, until Taylor (1959, 1960) produced definitive papers on the subject. Taylor defined the basic linear wave motions within the sheets, and wrote a general equation for the form of symmetrical sheets subject to gravity and pressure. A renewed interest in the problem followed Taylor's paper, and bibliographies of recent work now tend to be quite lengthy (see e.g. Huang 1967).

Recent work has resulted in descriptions of the shape of water bells under a variety of conditions; it has shown how the velocity deviates from radial uniformity under different circumstances; and it has been addressed to describing

† Present address: Engineering Research Department, Minnesota Mining and Manufacturing Company, St Paul, Minnesota 55112.

the sprays that occur after break-up. Much work has also been directed toward predicting the mechanisms of break-up in the spreading sheet but this has been less than conclusive in many respects. Dumbrowski, Fraser and their co-workers (e.g. 1962, 1963, 1964) have made significant studies which serve to expose wave motions of high velocity sheets, and which clarify the aerodynamic contribution of the surrounding air. Little has been done with slower moving sheets since the work of Savart (1833), and Bond (1935), and quantitative measurements of wave motions in the high-speed region are generally sparse.

The present study is an essentially experimental attempt to expand our understanding of break-up over several regimes that occur as the sheet velocity is increased. The effects of cylindrical geometry on wave motion of the sheet will also be examined using a linearized wave theory.

2. Experiment

Figure 1 shows the basic apparatus that we used to generate flat symmetrical sheets. Tap water was supplied at approximately 60 °F to a water bell maker consisting of $2\frac{3}{8}$ in. I.D. brass tube in which were affixed opposing, adjustable,

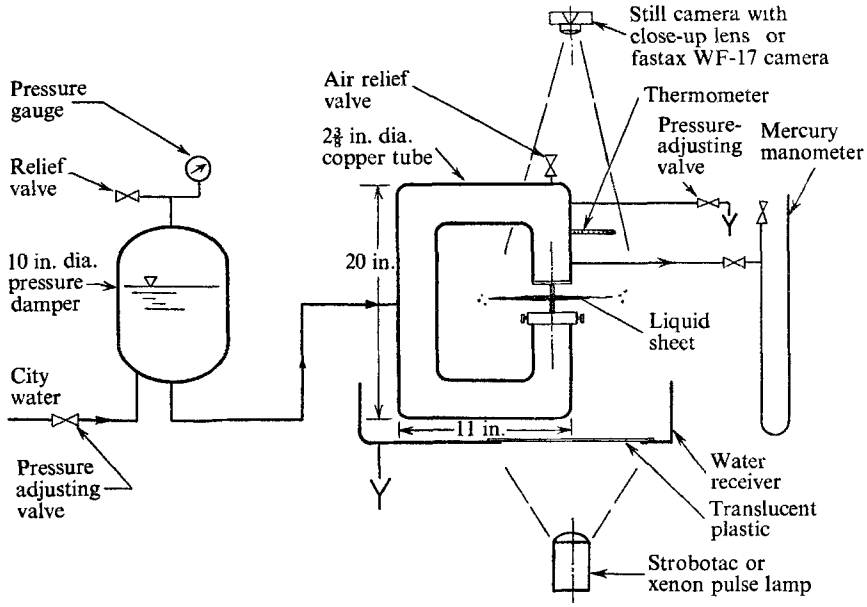

FIGURE 1. Schematic diagram of apparatus and photographic arrangement.

standard ASME orifices ranging from $\frac{1}{16}$ to $\frac{3}{16}$ in. in diameter. The jets passed into an air environment at a pressure of approximately 13·4 psia. Instrumentation provides for measurement of the jet velocity and for photographic observation of the sheets. Detailed descriptions of the experiments made on this apparatus are given by Huang, and we shall not repeat them here. The error of the photographic observations is intrinsically small, and its approximate magnitude will be evident from the photographs themselves. The exposure time of the

photographs ranges from 1 μs to 3 μs. High-speed motion pictures were taken at 6000 pictures per second.

The effect of internal viscous shear upon the liquid velocity in axisymmetric sheets is generally negligible (Lienhard & Newton 1966). The skin friction caused by the still air adjacent to the moving liquid sheet is also very small (Taylor 1959). Therefore, the radial velocity, U, throughout the expanding circular sheet will be assumed as constant in the following analysis.

3. The break-up regimes

Figure 2 presents the measured break-up radii of sheets in dimensionless form. The break-up radius r_b is non-dimensionalized with the orifice radius $\frac{1}{2}d$. The non-dimensional velocity has been squared so that it takes the form of a Weber number, $We = \rho U^2 d/\sigma$, where ρ is the liquid density and σ is the surface tension. The photographs, typical examples of which are shown in figure 3 (plate 1), illustrate the characteristics of the sheets at various Weber numbers.

In figure 2, we can readily see that the liquid sheets have three distinct break-up regimes. The first portion from $We \simeq 100$ to 500 represents a stable liquid sheet† regime. The liquid sheet has a nearly perfect circular edge. Figure 3(*a*) shows a liquid sheet ($We = 360$) in this regime; liquid beads are formed along the circular periphery. Our first high-speed motion pictures of the liquid sheet in this regime have shown that these beads moved along the periphery and became larger beads which are finally detached from the periphery to form droplets. The second portion from $We \simeq 500$ to 2000 represents a transition regime. From $We \simeq 500$ to 800, the liquid sheet forms a cusp-shaped edge. An example of a liquid sheet in this regime is shown in figure 3(*b*) ($We = 580$). Figure 3(*c*) is an enlarged view of a portion of figure 3(*b*), in which a liquid bead detached from the peak of a cusp edge is clearly indicated. In the critical zone $We \simeq 800$ to 1000, liquid sheets possess a maximum break-up radius. From $We \simeq 1000$ to 2000, the cusps on the edge of the liquid sheet diminish in size and the edge remains fairly circular; large-amplitude, antisymmetric wave‡ fronts can be seen. Figures 3(*d*) ($We = 880$) and 3(*e*) ($We = 1060$) show that small perturbations appear in portions near the edge of circular sheets.

The third portion, from $We \simeq 2000$ to 3×10^4, represents an unstable liquid sheet§ regime. Large-amplitude antisymmetric waves on the sheet are pronounced; the sheets flap with a flaglike motion. Figures 3(*f*) ($We = 2080$), 3(*g*) ($We = 4450$), 3(*h*) ($We = 8450$) and 3(*i*) ($We = 31{,}400$) show the progressive violence of perturbations on the liquid sheet as the Weber number increases. Steep wave fronts can be seen in all these figures, except figure 3(*i*), in which the disturbance is so large that no clear wave pattern can be observed. However,

† A 'stable liquid sheet' in this paper means that the sheet moves smoothly. Any disturbance on the sheet will be small and will decay radially.

‡ Waves in which the displacement of opposite surfaces of the sheet are in phase. (See Taylor 1959.)

§ An 'unstable liquid sheet' in this paper means that the sheet flaps with a flaglike motion. Any disturbance on the sheet will grow radially.

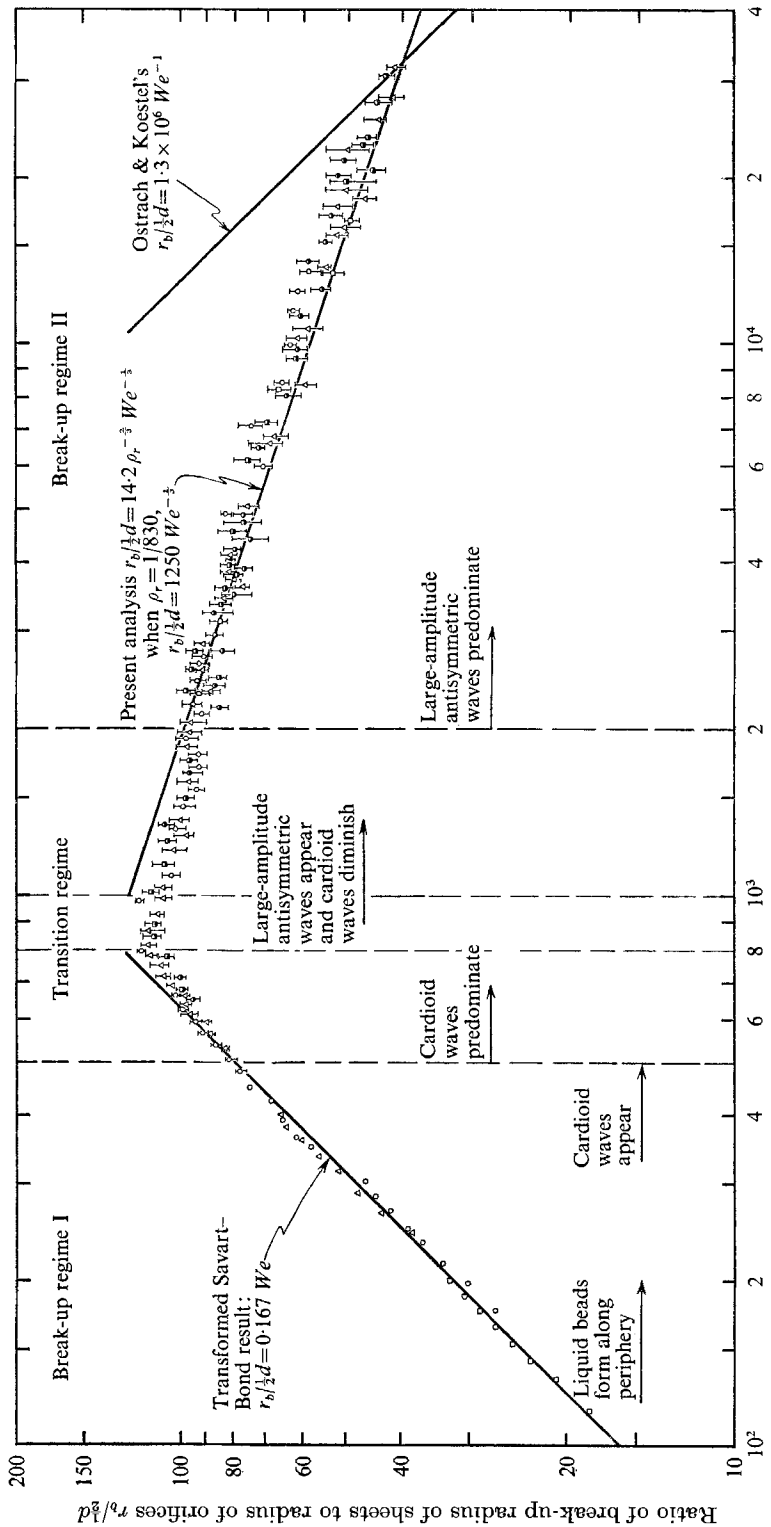

FIGURE 2. Relationship between the break-up radius of liquid sheets and the Weber number. □, $\frac{1}{16}$-in. dia. jets; ○, $\frac{3}{32}$; △, $\frac{1}{8}$; ■, $\frac{5}{32}$; ◑, $\frac{3}{16}$; ⊥, distance between upper bound (average radius where disintegration is complete) and lower bound (average radius where disintegration is first visible).

a complete disintegrated edge of the sheet can still be determined after observing several photographs taken at the same Weber number. Five high-speed motion pictures are taken in this regime to measure the wave speed which will be discussed later in §4. These three distinct regimes are designated as the break-up regime I, the transition regime, and the break-up regime II, respectively. The analysis of each regime will be presented in the subsequent sections.

(i) *First break-up regime*

In the first break-up regime, the liquid sheet is assumed free from any external disturbances. With this assumption, the inertia force exerted radially outward on the edge of the circular sheet is balanced by the inward radial and circumferential surface forces. The force balance on the edge of the circular liquid sheet is then

$$Q\rho U = 2(2\pi R\sigma) + \frac{\sigma}{R}(2\pi R h_b), \tag{1}$$

where R designates the maximum radial distance to which the moving sheet can extend, and h_b is the thickness at the edge of the circular sheet. The purpose of including the last term in (1) is to find out the approximate order of magnitude of the circumferential surface force which later has been found to be small and can be neglected in most cases. The flow rate Q can be obtained as

$$Q = 2\left(C_c\frac{\pi d^2}{4}\right)U = 2\pi R h_b U, \quad \text{or} \quad h_b = \frac{Q}{2\pi RU} = \frac{C_c d^2}{4R} \tag{2a, b}$$

where C_c is the coefficient of contraction. Substituting (2b) into (1), and solving for R, we obtain

$$\frac{R}{\frac{1}{2}d} = \frac{C_c}{8}We + \tfrac{1}{2}\left\{\left(\frac{C_c}{4}We\right)^2 - 2C_c\right\}^{\frac{1}{2}}. \tag{3}$$

The last term of (3) comes from the contribution of circumferential surface force. Unless the Weber number is of the order of magnitude 10 or less, the last term of (1) can be neglected. Then (3) becomes

$$\frac{R}{\frac{1}{2}d} = \frac{C_c}{4}We. \tag{4a}$$

Equation (4a) can also be written as

$$R = \frac{Q\rho U}{4\pi\sigma}, \tag{4b}$$

which is also obtained by Bond (1935).

If we take the average value of C_c obtained under low-pressure head by T. Hsieh (private communication), then $C_c = 0{\cdot}67$. Equation (4a) becomes

$$\frac{R}{\frac{1}{2}d} = \frac{r_b}{\frac{1}{2}d} = 0{\cdot}167\,We. \tag{4c}$$

Equation (4c) plotted in figure 2 shows agreement with the experimental data of regime I. We may call this regime the Savart–Bond regime.

When the liquid arrives at the edge, surface-tension force balances the inertia force, as if the liquid has reached a stagnation point. Actually, the liquid is continually flowing into and swelling the beads. A semicylindrical shape might

be assumed along the periphery of the sheet. Small disturbances in the radial direction will roughen the smooth cylindrical edge. If we assume that the classical Rayleigh jet instability mechanism prevails along the periphery, then the size of the beads should be in the same order of magnitude of λ_{max}, the optimum wavelength which corresponds to the maximum growth rate of the instability. Rayleigh's formula on λ_{max} can be then written as $\lambda_{max} = \sqrt{2}\pi h_b$. In the case of figure 3(*a*), $h_b \simeq 0{\cdot}00052$ in. and $\lambda_{max} \simeq 0{\cdot}00232$ in.

The smallest bead interval which can be measured from figure 3(*a*) is approximately 0·0061 in. and is two and one-half times the value obtained from the predicted value λ_{max}. Thus, the measured datum does give the right magnitude in comparison with the predicted value. Because h_b is very small, we could assume that equally spaced small beads originally existed, but, since they are continually merging, no equally spaced beads can be observed. Therefore, the sizes of the beads are several times larger than the predicted spacing λ_{max}. From observations of the enlarged photograph in figure 3(*c*) and the high-speed motion pictures, it is found that the droplets are formed when the liquid beads merge to form larger beads which eventually detach from the semicylindrical periphery. It is worth noting that a droplet is not a single Rayleigh's 'cylindrical bead', but the droplet actually results from the 'successive merging' of the many beads along the priphery.

Such a successive merging process has been observed by Lienhard & Wong (1963) for the case of vapour departure from small heated wires. Lienhard & Wong's prediction of λ_{max} (Rayleigh's λ_{max} plus gravitational effects) agrees very well with their measurements of the bubble spacing along the cylindrical heater when the heater diameter lies between 0·05 to 0·002 in. The bubbles become less evenly distributed when the diameter of the heater reduces in size. In one case, when the heater diameter is 0·001 in., they find that the wave behaviour is obscured by bubble mergings and 'oversized' bubbles depart from the heater.

This successive merging process could be of importance for the study of a drop formation from thin liquid films or from liquid jets of non-Newtonian fluids.†

(ii) *Transition regime*

When the Weber number of the liquid sheets goes beyond regime I, some small disturbances originate at the colliding point of the two jets. These disturbances initiated at the centre of the circular sheet propagate throughout the entire sheet. The cusp-shaped edge of the liquid sheet results from the presence of these disturbances and follows a more or less regular pattern. These small disturbances also exist in the first break-up regime, but usually they are too small to prevail, so the sheet appears to be nearly circular. Occasionally the cusp-shaped edge is visible in the first break-up regime.

Taylor (1959) very cleverly analyzed the small disturbances on liquid sheets when the sheets have constant velocity U. He concluded that, in the case of a sheet with a constant thickness h, a small disturbance on the sheet forms two

† An exaggerated example of the merging process can be seen in Goldin, Yerushalmi, Pfeffer & Shinnar (1969), in which the merging mechanism of beads along a viscoelastic jet is shown clearly in a sequence of high-speed motion pictures.

straight lines with angle $\sin^{-1}(2\sigma/\rho h U^2)^{\frac{1}{2}}$ between them. His experiment confirmed his theory. In the case of a circular expanding liquid sheet, a small disturbance in the centre of the sheet forms two cardioidal wave lines. These cardioidal wave lines are represented, in polar co-ordinates (r, θ), by

$$\frac{2r}{R} = 1 - \cos(\theta - \theta_0), \tag{5}$$

where R is the maximum possible radius, defined in (4*b*), and θ_0 is a constant introduced by integration, which represents the angular position measured from an arbitrary zero.

Taylor made the following experiment to confirm his analysis in the case of a circular expanding sheet: he allowed a jet directed vertically upwards to impinge on an impactor which had eight equally spaced radial nicks on its surface. A metal ring with its diameter smaller than the sheet was placed so that it intercepted the fluid before it reached the free edge. The resulting circular sheet had eight cardioid waves on the surface. These eight cardioid waves coincided with eight cardioid waves drawn from (5). Taylor did not go on further to observe the ragged edge which he had eliminated with the metal ring.

We believed that, in the first half of the transition regime, small disturbances initiated at the point of collision created many cardioid waves throughout the sheet. Such disturbances are usually so small that no cardioid waves on the surface are visible until the liquid reaches the edge. This edge follows the cardioid wave pattern as can be seen in the following experiment:

The liquid sheet in figure 4 (plate 4) is formed by the collision of two $\frac{5}{32}$ in. diameter jets at $We = 640$. The maximum radius R calculated from (4*c*) is 8·49 in. We use (5) to draw the 16 cardioid waves on the photograph. The cusp edge of the sheet generally coincides with the curves. How many cardioid waves exist on the surface is unknown. We may conclude that if we drew more cardioid wave lines on the surface, all the cusp edges will coincide with an appropriate cardioid wave line. The liquid beads merge along the cardioid wave lines tending toward the outer cusp points. This tendency of the beads to merge might have resulted from the radially flowing liquid pushing the merging beads outward. (Refer to figures 3(*b*) and 3(*c*).)

In the first half of the transition regime, the ragged periphery is generally close to R, with some discrepancy which results from the existence of the cardioid waves. The data for $We = 500$ to 800 in figure 2, show a small deviation from the predicted (4*c*).

When the characteristic break-up curve reaches its critical zone, which lies approximately between the Weber numbers 800 to 1000, liquid sheets generally are stable but are sensitive to any perturbation. No distinct cardioid wave edge can be observed. When the Weber number exceeds that of the critical zone, liquid sheets become slightly unstable. Antisymmetric waves propagate radially with growing amplitude. In the second half of the transition regime ($We \simeq 10^3$ to 2×10^3), the wave behaviour is the same as that in the second break-up regime, but is less pronounced.

(iii) *Second break-up regime*

When the Weber number exceeds approximately 2000, the liquid sheet is distinctly unstable. Observations by high-speed photography have shown that the upper and lower interfaces of the liquid sheet are so close that the sheet seemingly oscillates like a membrane. If we neglect the details of the liquid flow between the two interfaces of the sheet, we may assume that the flag-like wave motion of the liquid sheet is analogous to that of a moving vibrating membrane. Under this assumption, we have studied the two-dimensional constant-thickness membrane motion.

When the displacement of the membrane is assumed to be $\eta = a\exp[i(kx-\omega t)]$, where a is the maximum deviation from the unperturbed membrane, k is the wave-number, ω is the angular frequency, x is the co-ordinate of the membrane moving direction and t is the time. The derivations of this linear wave motion are straightforward, and are given in Huang (1967). The results are reported as follows:

$$\omega = \frac{Uk \pm k\left[\frac{2\sigma}{\rho h}+\frac{4\sigma\rho_a}{\rho^2h^2k}-\frac{2\rho_aU^2}{\rho hk}\right]^{\frac{1}{2}}}{1+\frac{2\rho_a}{\rho hk}}, \tag{6}$$

$$\lambda_{\max} = \frac{2\pi}{k_{\max}} \simeq \frac{4\pi\sigma}{\rho_aU^2}\left\{1+2\left(\frac{\rho U^2h}{\sigma}\right)^{-1}+\left(\frac{\rho U^2h}{\sigma}\right)^{-2}\right\}^{-1}, \tag{7}$$

and

$$\omega_i|_{\max} \simeq \frac{\rho_aU^2}{(2\rho h\sigma)^{\frac{1}{2}}}\left[1-4\left(\frac{\rho U^2h}{\sigma}\right)^{-1}\right]^{\frac{1}{2}}\left[1+4\left(\frac{\rho U^2h}{\sigma}\right)^{-1}\right]^{-1}, \tag{8}$$

where $\lambda_{\max}$ and $k_{\max}$ are, respectively, the wavelength and the wave-number for maximum instability, $\omega_i|_{\max}$ is the maximum growth rate of unstable waves, ρ_a is the density of the ambient air and h is the thickness of the sheet. When $\rho U^2h/\sigma \gg 1$, (4) and (8) can be approximated as

$$\lambda_{\max} \simeq \frac{4\pi\sigma}{\rho_aU^2}, \quad \omega_i|_{\max} \simeq \frac{\rho_aU^2}{(2\rho h\sigma)^{\frac{1}{2}}}. \tag{9a,b}$$

The above two relations were also obtained in Squire (1953), where the velocity potential between two interfaces of the sheet is considered. Two different approaches giving the same result might indicate that it is legitimate to neglect the details of the liquid movement between two interfaces of thin liquid sheets.

The prediction of the break-up length of axisymmetric liquid sheets will be drawn from the analogy of the prediction of the break-up length of cylindrical jets (e.g. Weber 1931). The magnitude of the disturbance of unstable waves is simply

$$|\eta| = ae^{\omega_i t}. \tag{10}$$

The break-up distance r_b can now be approximated as

$$r_b \simeq \frac{c_1U}{\omega_i|_{\max}}. \tag{11}$$

The parameter c_1 in (11), following (9), is $\ln(\eta_b/a)$. The subscript b indicates variables at the break-up point. Weber in his study of the break-up mechanism

of cylindrical jets reported $\ln(\eta_b/a) = 12$, a value which has been accepted by some later investigators. Ostrach & Koestel (1965), who studied the break-up length of annular liquid film inside ducts, and Fraser *et al.*, who studied the drop size formed from the fan spray sheet, all decided that $\ln(\eta_b/a) = 12$ is a universal constant, and can be applied in any geometrical configuration. Grant & Middleman (1966) reported on the instability of Newtonian jets, however, and revealed that $\ln(\eta_b/a)$ is not a constant value, but a function of the Weber number and Reynolds number, and has to be determined experimentally in every case.

The huge value of the ratio (η_b/a) seems to defy any physical interpretation. We would just conclude that r_b is proportional to U and inversely proportional to $\omega_i|_{\max}$. The constant c_1 has to be determined from experiments.

By substituting (9*b*) into (11), and letting $h = h_b = C_c d^2/4r_b$, we obtain

$$\frac{r_b}{\frac{1}{2}d} = c_1^{\frac{2}{3}}(4C_c)^{\frac{1}{3}}(\rho_r)^{-\frac{2}{3}}We^{-\frac{1}{3}}. \tag{12}$$

At laboratory room temperature, 71 °F, the air density $\rho_a = 0{\cdot}00234$ lbm/ft^3. The density of the supply water is 1·94 lbm/ft^3. In this case the density ratio $\rho_r = \rho_a/\rho = 1/830$. When we take the average value of C_c for the higher Weber number from Hsieh, $C_c \simeq 0{\cdot}65$. If we choose $c_1 = 33$, we find that (12) agrees very well with the experimental data. By substituting all above quantities into (12), a semi-empirical formula can be written

$$\frac{r_b}{\frac{1}{2}d} = 14{\cdot}2\rho_r^{-\frac{2}{3}}We^{-\frac{1}{3}}, \quad \text{or} \quad \frac{r_b}{\frac{1}{2}d} = 1250\,We^{-\frac{1}{3}}. \tag{13a,b}$$

Equation (13*b*) plotted on figure 2 agrees well with the measured break-up radii at the break-up regime II, and shows a small deviation from the data in the second half of the transition regime.

Ostrach & Koestel have also developed an equation to predict the break-up of liquid film at high Weber's number. Their result can be rewritten as

$$\frac{r_b}{\frac{1}{2}d} = (1{\cdot}3 \times 10^6)\,We^{-1}. \tag{14}$$

If we plot (14) in figure 2, we can see that, within the limits of the pressure head in the present experiment, (14) does not agree with our data.

4. Effects of cylindrical geometry on wave motion

The cylindrical geometry apparently has its effect in the propagation of anti-symmetric waves on the sheet. In §4, we shall attempt to analyze the motion of the axisymmetric membrane with decreasing thickness as an analogue to the wave motion of circular expanding liquid sheets.

The liquid mass at each radial distance is conserved. We can, therefore, treat the decreasing thickness of the liquid sheet as radially decreasing density. Then the equation of motion is

$$\left(\rho\frac{r_0^2}{r}\right)\frac{d^2\eta}{dt^2} = 2\sigma\left(\frac{\partial^2\eta}{\partial r^2} + \frac{1}{r}\frac{\partial\eta}{\partial r}\right) - 2\rho_a\frac{\partial\phi}{\partial t} \quad \text{at} \quad z = 0, \tag{15}$$

where $r_0 = \sqrt{C_c}\frac{1}{2}d$ is the radius of the jets at the colliding point, ϕ is the velocity potential of the surrounding gas, z is the co-ordinate in the membrane displacement direction, and d^2/dt^2 on the left side of (15) is the total derivative.

It is unlikely that we can simultaneously solve (15), the kinematic condition $\partial\eta/\partial t = -\partial\phi/\partial z$ at $z = 0$, and the Laplace equation† of ϕ in cylindrical co-ordinates, as we have done in the case of two-dimensional, constant-thickness sheet. However, the displacement of the liquid sheet, rather than the surrounding gas, is the object of our interest. If we can find a proper expression for ϕ in terms of η, and substitute this expression into (15), then we shall be able to solve for the displacement η explicitly, and interpret the behaviour of the solution.

Let us assume

$$\phi(r, z, t) = \overline{\phi}(r, t)\, e^{-k'z}, \tag{16}$$

where k' is a decay factor. In two-dimensional analysis, the decay factor k' is independent of x and t; but, in a cylindrical co-ordinate problem, k' can be a slowly varying function of r. For simplicity, we shall assume that k' is independent of r and t. Applying (16), and the kinematic boundary condition, we can eliminate ϕ in (15). Also, by introducing the non-dimensional variables,

$$\overline{\eta}(X, \tau) = \frac{\eta(r, t)}{r_0}, \quad X = \frac{r}{r_0} \quad \text{and} \quad \tau = \frac{U}{r_0}t, \tag{17}$$

and the non-dimensional parameters,

$$\alpha = \frac{2\sigma}{\rho U^2 r_0} = \frac{4}{\sqrt{C_c}\, We} \quad \text{and} \quad \beta = \frac{2\rho_a}{\rho k' r_0}, \tag{18a,b}$$

into (15), we get

$$(1-\alpha X)\frac{\partial^2\overline{\eta}}{\partial X^2} - \alpha\frac{\partial\overline{\eta}}{\partial X} + 2\frac{\partial^2\overline{\eta}}{\partial X\,\partial\tau} + (1+\beta X)\frac{\partial^2\eta}{\partial\tau^2} = 0. \tag{19}$$

To determine the parameter β, we ought to be able to determine k'. Since we cannot evaluate k' directly in the cylindrical configuration, we would like to approximate k'. In the case of the two-dimensional, constant-thickness liquid sheet, the decay factor of the perturbation on the surrounding gas k' is the same as the wave-number k. From (7), we have found that $k_{\max} \simeq \rho_a U^2/2\sigma$ is the wave-number at the maximum growth rate. To be able to solve (19), which in turn can provide some knowledge of the wave behaviour due to the effect of cylindrical geometry when the liquid sheet is in the unstable regime II, we shall assume that

$$\beta \simeq \frac{2\rho_a}{\rho k_{\max} r_0} = \frac{8}{\sqrt{C_c}\, We} = 2\alpha. \tag{20}$$

When the liquid sheet is in the unstable regime II, the range of We is of the order of magnitude 10^3 to 10^4; therefore, both α and β are of the same order of magnitude and both are much less than one.

The coefficients of the differential equation (19) are independent of time. We can, therefore, assume

$$\overline{\eta}(X, \tau) = \hat{\eta}(X)\exp(-i\overline{\omega}\tau), \tag{21}$$

† This is the classical Kelvin–Helmholtz model (see e.g. Miles 1957).

where the dimensionless angular frequency $\bar{\omega} = (r_0/U)\omega$. By substituting (20) and (21) into (19), and again by using the transformation,

$$\hat{\eta}(X) = Z(X)\exp\left(\frac{1}{2}\int\frac{\alpha+2i\bar{\omega}}{1-\alpha X}dX\right), \tag{22}$$

we can transform (19) into $$\frac{d^2Z}{dX^2} - \bar{\omega}^2\alpha XZ = 0. \tag{23}$$

The dimensionless displacement function can then be approximated as

$$\bar{\eta}(X,\tau) = c_2 Z(X)\exp\{i\bar{\omega}(X-\tau)\}, \tag{24}$$

where c_2 is a constant. Equations (23) and (24) are obtained when terms of smaller order of magnitude have been neglected.

The solution of (23) is simply an Airy function. However, when the liquid sheet is unstable, $\bar{\omega}$ possesses both a real and an imaginary part. The behaviour of the Airy function for a complex argument is complicated. We therefore have applied the WKBJ (Wentzel, Kramers, Brillouin and Jeffreys) method (see, for example, Mathews & Walker 1964, p. 26), to give the following approximate solution:

$$Z(X) \simeq X^{-\frac{1}{4}}\{a_1\exp(-\tfrac{2}{3}\bar{\omega}\sqrt{\alpha}X^{\frac{3}{2}}) + b_1\exp(\tfrac{2}{3}\bar{\omega}\sqrt{\alpha}X^{\frac{3}{2}})\}. \tag{25}$$

Combining (24) and (25), we have thus found an approximation to the general solution of the displacement $\bar{\eta}$:

$$\bar{\eta}(X,\tau) = X^{-\frac{1}{4}}(a_1\exp(-\tfrac{2}{3}\bar{\omega}\sqrt{\alpha}X^{\frac{3}{2}}) + b_1\exp(\tfrac{2}{3}\bar{\omega}\sqrt{\alpha}\,X^{\frac{3}{2}}))\exp\{i\bar{\omega}(X-\tau)\}, \tag{26}$$

where c_2 has been absorbed into constants a_1 and b_1. Equation (26) is true in any region where X is greater than 40. Our experimental observations indicate that in the break-up regime II, antisymmetric waves are pronounced only at approximately $X > 40$. Hence, (26) is an acceptable approximation.

In this unstable break-up regime II, $\bar{\omega}$ is complex. The outgoing wave can then be represented by setting $\bar{\omega} = \bar{\omega}_r + i\bar{\omega}_i$, and rewriting (26) as

$$\bar{\eta}(X,\tau) = b_2 X^{-\frac{1}{4}}\exp(\theta_1 + i\theta_2), \tag{27}$$

where $$\theta_1 = \tfrac{2}{3}\bar{\omega}_r\sqrt{\alpha}\,X^{\frac{3}{2}} - \bar{\omega}_i X - \bar{\omega}_i\tau, \quad \theta_2 = \tfrac{2}{3}\bar{\omega}_i\sqrt{\alpha}\,X^{\frac{3}{2}} + \bar{\omega}_r X - \bar{\omega}_r\tau. \tag{28}$$

Equation (27) is a distorted progressive wave solution, indicating that the wave amplitude will grow exponentially along the radial direction.

The wave speed can be obtained by differentiating θ_2 with respect to τ and setting the result equal to zero

$$\frac{\partial\theta_2}{\partial\tau} = \bar{\omega}_i(\alpha X)^{\frac{1}{2}}\frac{dX}{d\tau} + \bar{\omega}_r\frac{dX}{d\tau} - \bar{\omega}_r = 0.$$

Then the wave speed, $\bar{C} = dr/dt + U\,dX/d\tau$, is

$$\bar{C} = \frac{U}{1 + (\bar{\omega}_i/\bar{\omega}_r)(\alpha X)^{\frac{1}{2}}} \simeq U\left(1 - \frac{\bar{\omega}_i}{\bar{\omega}_r}(\alpha X)^{\frac{1}{2}}\right). \tag{29}$$

We do not know the values of $\bar{\omega}_i$ and $\bar{\omega}_r$; generally $\bar{\omega}_i$ is less than $\bar{\omega}_r$. In the previous analysis of wave motion on constant thickness sheets, we have obtained

two formulas for $\overline{\omega}_r$ and $\overline{\omega}_i$ in (6). The ratio of $\overline{\omega}_i/\overline{\omega}_r$, in that case, has been found to be approximately 0·9 for We in $O(10^3)$ and 0·3 for We in $O(10^4)$. To acquire some idea of how the wave speed changes along the radial direction, we shall assume $\overline{\omega}_i/\overline{\omega}_r \simeq 1$ and set (29) as

$$\overline{C} \simeq U\left\{1-\left[\frac{4r/\frac{1}{2}d}{C_c\,We}\right]^{\frac{1}{2}}\right\}. \tag{30}$$

The following experimental data will be presented here to be compared with the approximate expression of (30). The wave speed for the region, from the first visible wave-front to the edge, was measured from the top view high-speed motion pictures, while the pictures were projected in a microfilm reader. The distance travelled by the wave-front, plotted against the consecutive frames of the high-speed motion pictures forms a time-displacement diagram. The slopes of the curve which connects all the data points are the speeds of the wave at each specific radial position. The wave speeds, in the case of the Weber numbers 2250, 4450, 7210, 10 300 and 16 000, against the dimensionless radial direction, $r/(\frac{1}{2}d)$, are plotted in figure 5. In each motion picture, three data lines are taken from three different portions of the 100-foot-long motion film. The uncertainty on the initial and the final data lines denotes the several possible curves of different slopes which can be drawn through the time-displacement diagram.

The wave speed equation (30) has been plotted as a dash-dot line in figure 5. We see that (30) represents fairly well the terminal velocity of low We (figures 5(*a*) and (*b*)) while the wave is still linear. When We is very high (figures 5(*c*), (*d*) and (*e*)), the non-linear wave mechanism predominates on these flapping sheets. The present linear wave theory is no longer valid.

One interesting point should be noted here. If we superpose the velocity of the liquid sheet, U, on the speed of sound, $(2\sigma/\rho')^{\frac{1}{2}}$, obtained from the classical analysis of the vibrating membrane, then the absolute wave speed is simply $U \pm (2\sigma/\rho')^{\frac{1}{2}}$. When we substitute $\rho' = \rho(C_c d^2/4r)$, and take the minus sign of the above equation, we obtain the same wave speed equation as in (30). This may indicate that, at the condition when $\overline{\omega}_i = \overline{\omega}_r$, effects of cylindrical geometry on wave motion are related only to the radially decreasing liquid sheet thickness.

5. Concluding remarks

The major results of this investigation are presented in figure 2 where the three break-up regimes and the dynamic behaviour in each regime are concisely reported. The shape of the characteristic break-up curve of the liquid sheet is similar to that of the break-up curve of the cylindrical jet.

We believe that for every liquid, axisymmetric sheets have a break-up curve, the shape of which is similar to that of the break-up curve of water sheets in figure 2. Knowing the transition regime of the characteristic break-up curve, we will be able to determine the conditions for producing a stable sheet or an unstable sheet of a particular liquid. For some applications, such as film coating, a stable sheet is required, whereas for others, such as spraying, an unstable sheet is preferred.

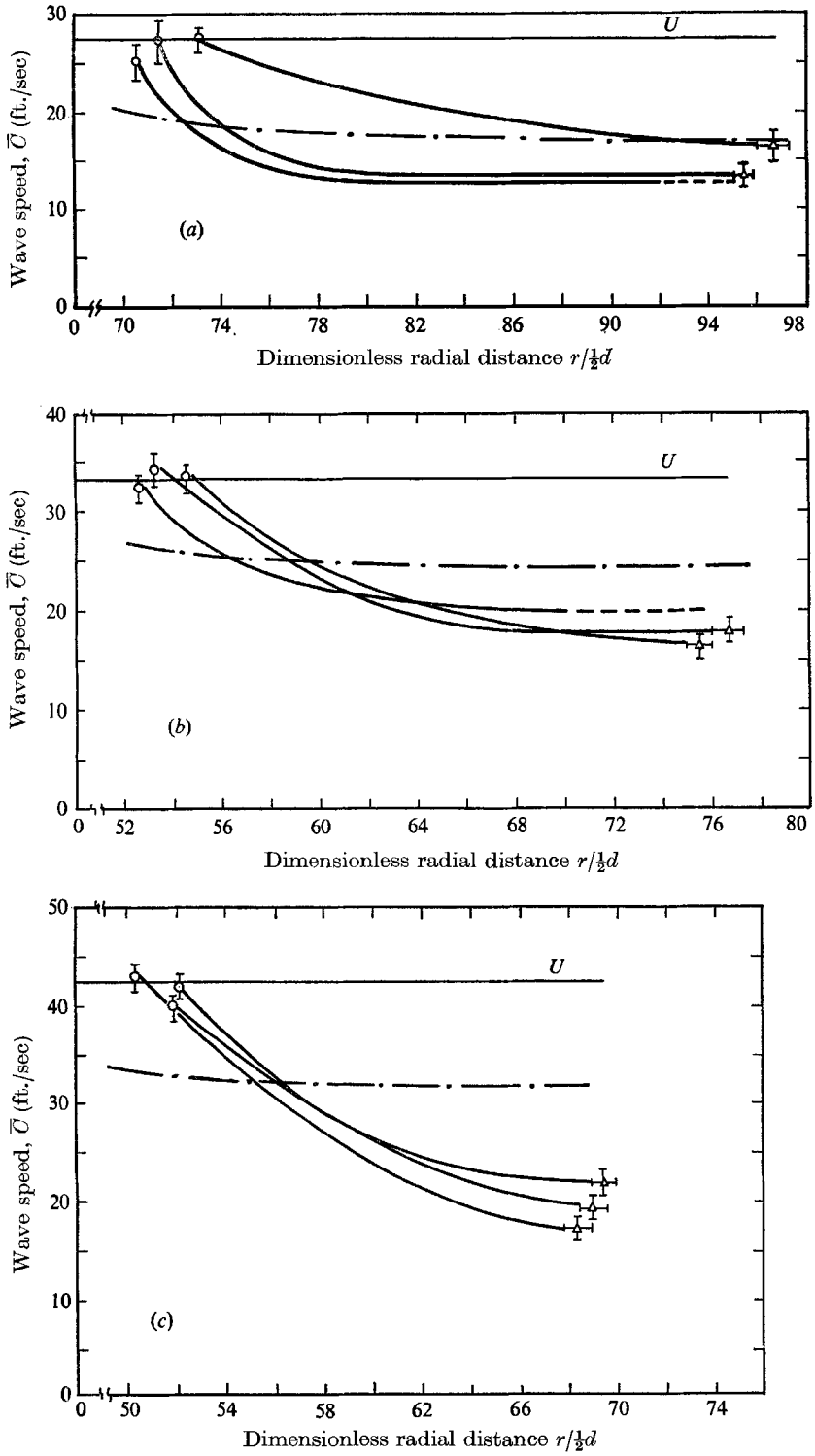

FIGURE 5 (*a*)–(*c*). For legend see next page.

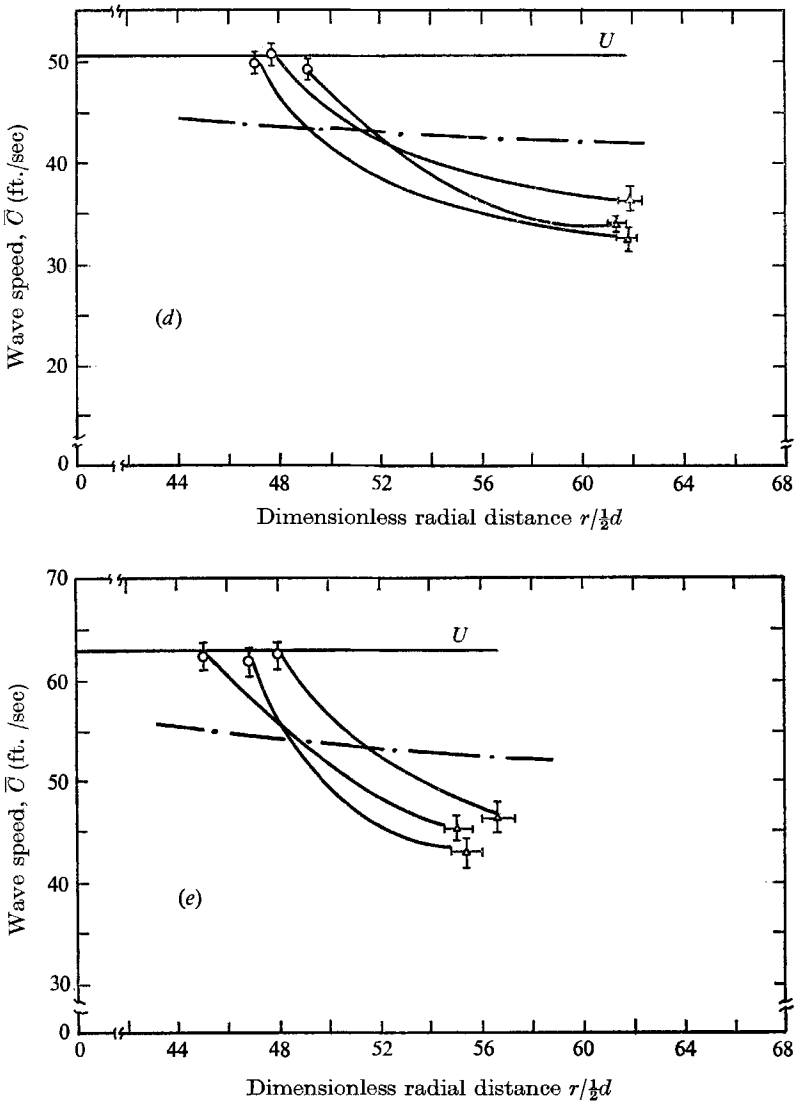

FIGURE 5. Wave speed *vs.* radial distance. (*a*) We = 2250; (*b*) 4450; (*c*) 7210; (*d*) 10 300; (*e*) 16 000. ○, first appearance of a wave front; △, the edge of the sheet; ——, an unidentified wave front; —·—·, predicted by linearized theory; I, range of uncertainty.

The present linear wave theory does not completely interpret the wave behaviour of the liquid sheet. The non-linear, shallow-water wave theory, or the non-linear vibrating membrane theory, may indicate a new approach to the understanding of the steep wave front behaviour of the thin liquid sheet in the high Weber number regime.

I am grateful to Professor J. H. Lienhard for calling my attention to the distinction between a single Rayleigh 'cylindrical bead' and a droplet resulting from 'successive merging'. I am thankful to Professors Lienhard and S. C.

Lowell for the stimulating discussions throughout this study. Mr H. D. Howard helped to obtain the informative photographs. This work was largely supported by the Research Center of the College of Agriculture, Washington State University.

REFERENCES

BOND, W. N. 1935 *Proc. Phys. Soc.* **47**, 549.

DOMBROWSKI, N. & HOOPER, P. C. 1962 *Chem. Engng Sci.* **17**, 291.

DOMBROWSKI, N. & HOOPER, P. C. 1964 *J. Fluid Mech.* **18**, 392.

DOMBROWSKI, N. & JOHNS, W. R. 1963 *Chem. Engng Sci.* **18**, 203.

FRASER, R. P., EISENKLAM, P., DOMBROWSKI, N. & HASSON, D. 1962 *A.I.Ch.E.J.* **8**, 672.

GOLDIN, M., YERUSHALMI, J., PFEFFER, R. & SHINNAR, R. 1969 *J. Fluid Mech.* **38**, 689.

GRANT, R. P. & MIDDLEMAN, S. 1966 *A.I.Ch.E.J.* **12**, 669.

HUANG, J. C. P. 1967 Research Division, College of Engineering, Washington State University, Bulletin 306.

LIENHARD, J. H. & NEWTON, T. A. 1966 *Z. angew Math. Phys.* **17**, 348.

LIENHARD, J. H. & WONG, P. T. Y. 1963 *J. Heat Transfer*, **86**, 220.

MATHEWS, J. & WALKER, R. L. 1964 *Mathematical Methods of Physics*. New York: Benjamin.

MILES, J. W. 1957 *J. Fluid Mech.* **3**, 185.

OSTRACH, S. & KOESTEL, A. 1965 *A.I.Ch.E.J.* **11**, 294.

SAVART, F. 1833 *Ann. Chem. Phys.* **59**, 55, 113.

SQUIRE, H. B. 1953 *Br. J. Appl. Phys.* **4**, 167.

TAYLOR, G. I. 1959 *Proc. Roy. Soc.* A **253**, 289, 296, 313.

TAYLOR, G. I. 1960 *Proc. Roy. Soc.* A **259**, 1.

WEBER, C. 1931 *Z. angew Math. Mech.* **2**, 136.

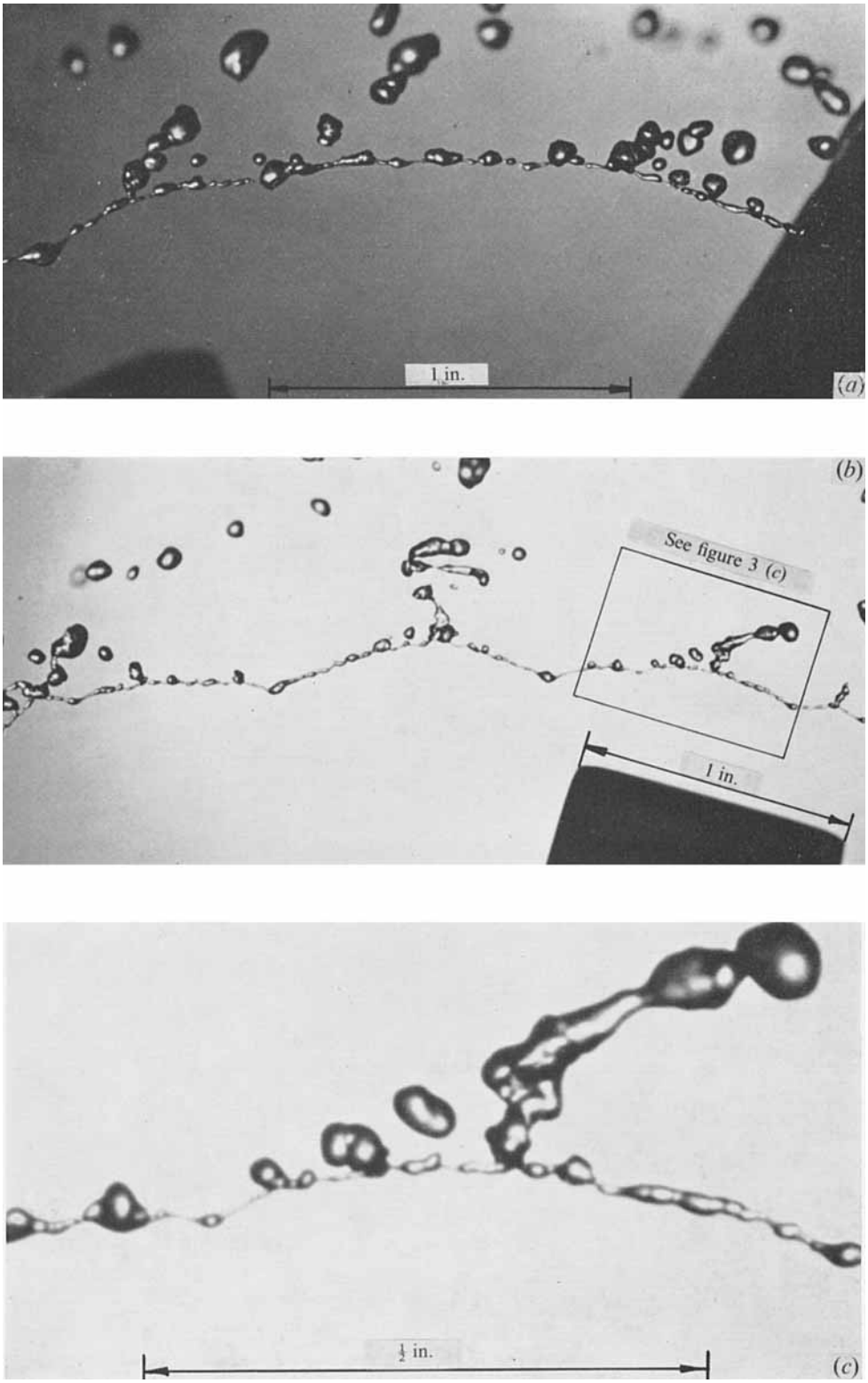

FIGURE 3 (*a*)–(*c*). For legend see plate 3.

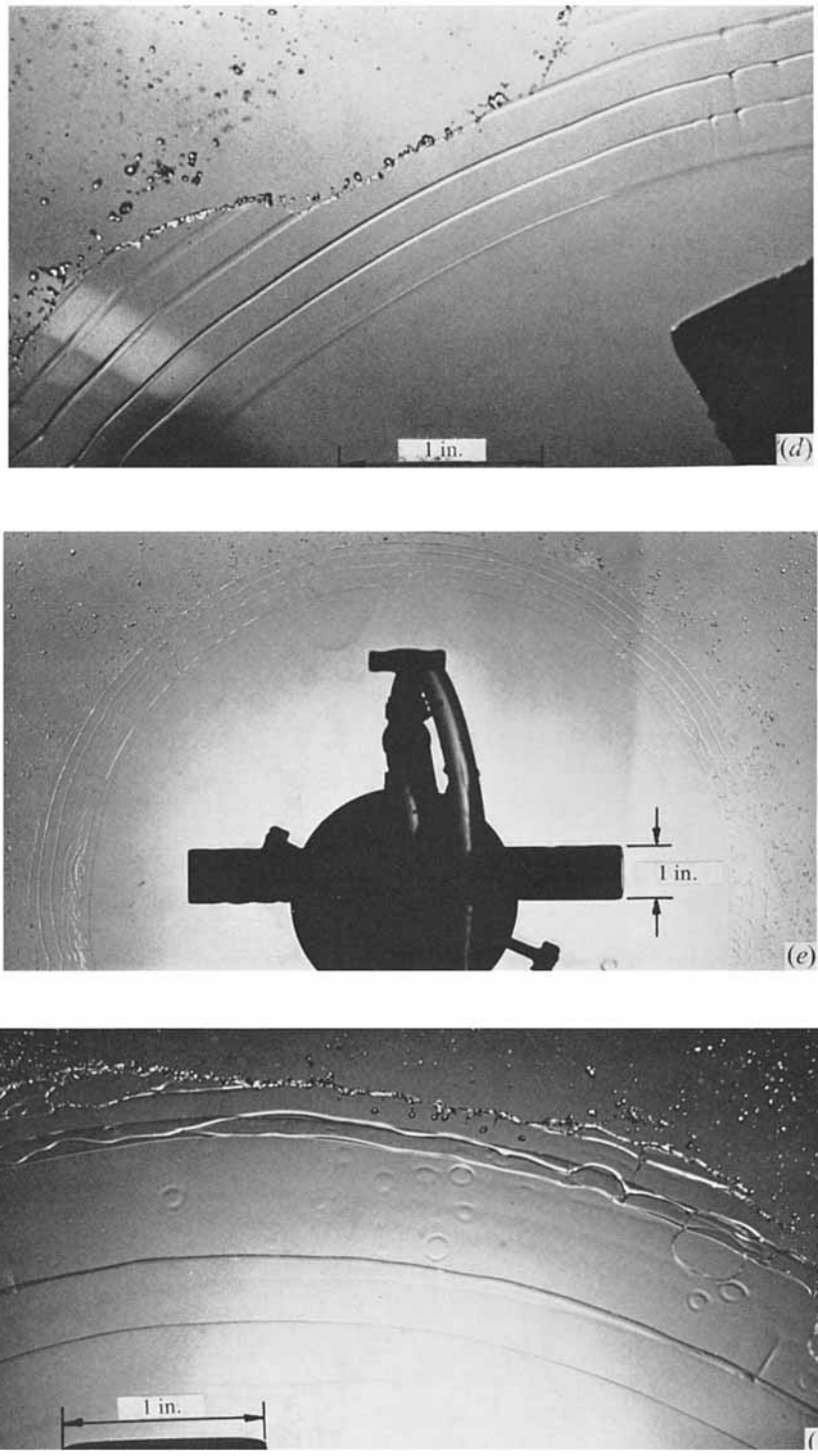

FIGURE 3 (*d*)–(*f*). For legend see facing page.

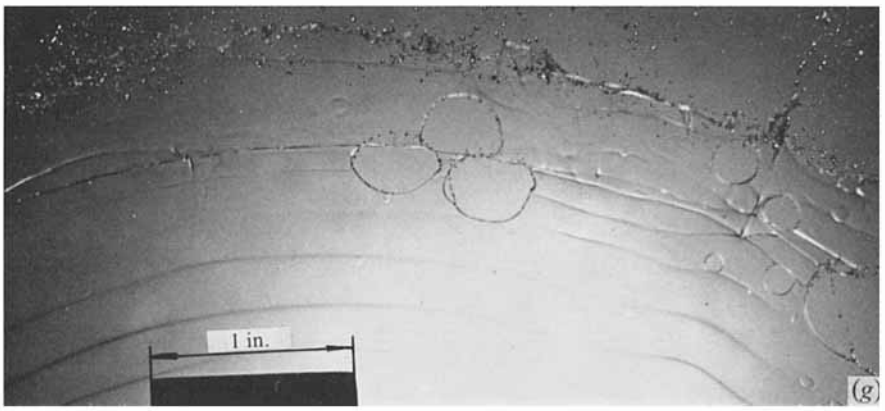

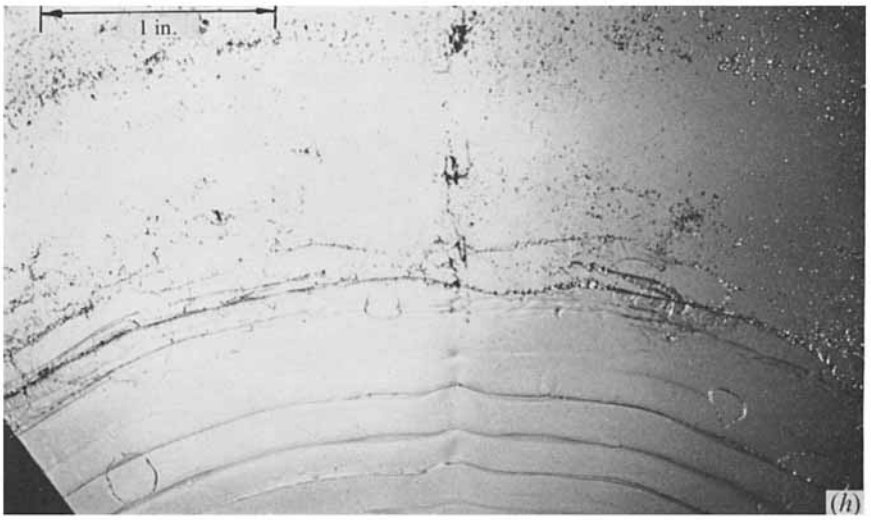

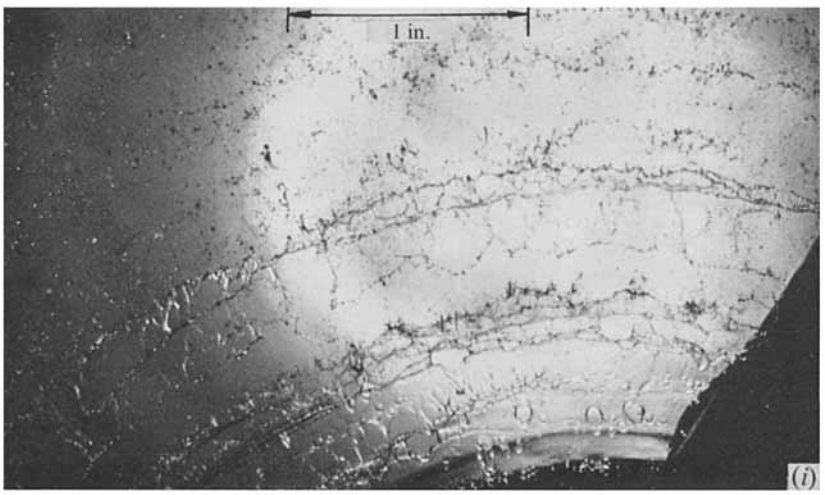

FIGURE 3. Top view of water sheets formed by the co-axial collision of two equal-diameter jets under various pressure heads. (*a*) We = 360; (*b*) 580; (*c*) 580; (*d*) 890; (*e*) 1060; (*f*) 2080; (*g*) 4450; (*h*) 8450; (*i*) 31 400.

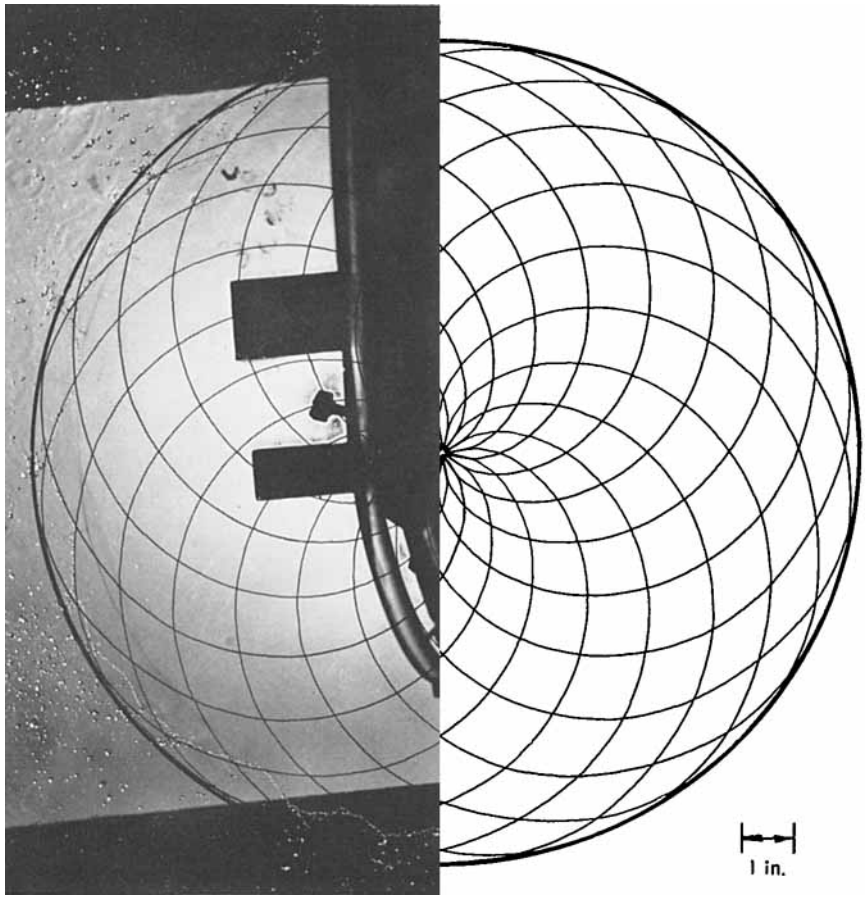

FIGURE 4. Cardioid waves at the edge of a sheet compared with drawn cardioid waves.